Chinese Journal of Chemical Engineering 90 (2026) 45–58

Contents lists available at ScienceDirect

Chinese Journal of Chemical Engineering

journal homepage: www.elsevier.com/locate/CJChE

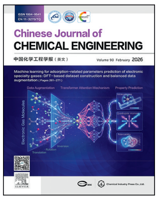

Full Length Article

Integrated scrubber for enhanced purity of alkaline electrolyzed water system

Yufei Xie [1], *, Wu Qin [1], [2], *, Xianbin Xiao [1], Zongming Zheng [1]

[1] *School of New Energy, North China Electric Power University, Beijing 102206, China*
[2] *School of Engineering, China University of Petroleum-Beijing at Karamay, Karamay 834000, China*

ARTICLE INFO

Article history:
Received 20 June 2025
Received in revised form
15 August 2025
Accepted 16 September 2025
Available online 25 November 2025

Keywords:
Hydrogen production
Alkaline water electrolysis
System simulation
Purity of H_2

ABSTRACT

This study addresses gas entrainment challenges in alkaline water electrolysis (ALK) hydrogen production through an integrated scrubbing-purification solution and establishes a thermodynamic-electrochemical multi-physics coupled model to optimize system performance. A complete hydrogen production system model with a hydrogen production capacity of 2.5 $m^3 \cdot h^{-1}$ was established, focusing on the synergistic effect of key parameters such as current density (0.1–0.4 $A \cdot cm^{-2}$), operating pressure (0.7–0.9 MPa) and electrolysis temperature (40–80 °C) on system performance. The study shows that compared with the traditional system, the system coupled with the scrubbing and purification device can increase the hydrogen purity from 94.5% to more than 99.5%, meeting the industrial storage and transportation standards. Parametric analysis reveals that elevated temperatures enhance water conversion efficiency but inversely affect purity, while increased pressure improves purity linearly. A critical current density equilibrium point was identified, below which the integrated system outperforms traditional setups in efficiency. The Aspen plus model proves that the efficiency difference between the integrated system and the traditional system is only at the order of 10^{-5}. This work resolves the efficiency-purity trade-off in ALK systems, offering a viable pathway for industrial-scale high-purity hydrogen production. Future studies should integrate techno-economic assessments to advance scalable, sustainable electrolysis technologies.

1. Introduction

The proliferation of renewable energy sources (RES) has intensified challenges in power grid stability due to their intermittent nature at large-scale deployment [1]. Hydrogen, as a versatile energy vector, has gained prominence in global energy transition strategies for its capacity to address energy storage and grid balancing needs. Among hydrogen production technologies, alkaline water electrolysis (ALE) technology has become one of the main ways to produce hydrogen with its mature technical system and relatively low cost [2]. However, ALE systems face operational inefficiencies, particularly potassium hydroxide (KOH) entrainment in hydrogen product streams during gas-liquid separation [3]. This issue reduces hydrogen purity, compromises product quality, and exacerbates operational risks, including equipment corrosion and reduced component lifespans, thereby increasing maintenance costs. Mitigating KOH entrainment while preserving system efficiency and purity has become a critical focus for ALE optimization.

Currently, a substantial body of research has integrated renewable energy sources with alkaline water electrolysis (AWE) and has delivered comprehensive case studies coupled with techno-economic assessments. Kiaee *et al.* leveraged field data from a 24 kW pressurized AWE unit at the Porsgrunn hydrogen refueling station in Norway to quantify the efficiency evolution under fluctuating wind and solar conditions, thereby providing experimental foundations for real-time control strategies of hybrid systems [4]. Sakas *et al.* [5] developed a zero-dimensional dynamic mass-and-energy balance white-box model (Simulink-MATLAB) for a 3 MW industrial AWE plant; validation against operational data yielded a thermal-state prediction accuracy of 98.7% and a nominal Faradaic efficiency of 86%, with dominant losses attributed to shunt currents (11.2%) and overpotentials (20.3%),

---

* Corresponding authors.

E-mail addresses: 15738780841@163.com (Y. Xie), qinwu@ncepu.edu.cn (W. Qin).

https://doi.org/10.1016/j.cjche.2025.09.029
1004-9541/

furnishing a reliable tool for scale-up design and optimization. Hassan *et al.* [6] combined 1-min-resolution annual wind and solar resource data with genetic algorithms and a life-cycle cost model to perform capacity matching and economic optimization of a 2.5 MW wind-plus-2.5 MW PV-driven AWE hydrogen production system. Jang *et al.* [7] constructed an Aspen Plus full-flowsheet model encompassing the stack and balance-of-plant (BOP), coupling a zero-dimensional electrochemical routine *via* a solid-phase subroutine to systematically quantify the impact of operating pressure on system performance. Zheng *et al.* [8] devised a refined model for an off-grid wind–multi-stack AWE system that incorporates load-efficiency mapping, cold/hot start dynamics, and thermal management, and proposed a rolling-horizon optimization strategy for wind power allocation. Bhattacharyya *et al.* [9] combined thermodynamic analysis with a five-parameter single-diode PV model and annual solar irradiance data for Mumbai to complete the conceptual design and performance evaluation of a stand-alone PV-AWE hydrogen system . Shin *et al.* [10] employed machine learning to forecast offshore wind power, fused 1-h-resolution PV and onshore wind measurements, and established an AWE/PEMWE hybrid model accounting for part-load efficiencies to conduct a life-cycle techno-economic assessment of six 100 MW-class renewable-to-electrolysis scenarios. Yang *et al.* [11] elucidated the coupled transport-reaction phenomena within AWE *via* CFD and designed single- and multi-step MINLP scheduling strategies under a hybrid PV-grid scenario, optimizing hydrogen production plans with a 15-min rolling horizon. Lee *et al.* [12] developed a self-powered water-electrolysis hydrogen system by coupling a carbon-black/cellulose sponge–based evaporation-hydrovoltaic module with an alkaline electrolyzer. Aboukalam *et al.* [13] formulated a dynamic differential-algebraic model of an alkaline water-electrolysis unit grounded in thermochemical conservation principles, discretized it *via* orthogonal collocation finite-element methods into an algebraic system, and optimized its load profile over an entire year using hourly electricity-price curves as input. Lai *et al.* [14] built a 5 kW PEM electrolysis test rig synergistically powered by a PV-PV/T array and a PCM hot-water tank, demonstrating through a four-mode operating strategy that dynamic thermal management and electrolyte preheating markedly enhance the efficiency of small-scale solar-to-hydrogen conversion. Zhou *et al.* [15] constructed a capacity-allocation model for a wind–PV–CSP-coupled renewable hydrogen system, minimized daily operating costs with the CPLEX solver across six scenarios, and showed that the integrated system achieves >99% renewable-energy utilization with the lowest cost and best prospects. Huang *et al.* [16] combined life-cycle assessment and cost analysis to evaluate the environmental and economic sustainability of PEM water electrolysis under standalone PV, off-grid PV-plus-battery, and grid-connected PV configurations in five Chinese provinces. Xu *et al.* [17] used Aspen Plus to model and integrate corn-straw gasification, alkaline water electrolysis, methanol and DME synthesis, and a supercritical CO_2 Brayton cycle into a novel poly-generation system, comprehensively evaluating it *via* thermodynamic, exergy, and economic analyses. Wang and Li [18] established and validated an Aspen Plus V11 model of a CHP-M system that integrates biogas power, PEM electrolysis, and CO_2-to-methanol catalysis, demonstrating its viability through multi-criteria assessment of thermodynamics, economics, and carbon footprint, thus offering a practical route for waste-heat valorization and CO_2 utilization in biogas plants.

Although the Ulleberg model accurately reflects the polarization curves of alkaline electrolyzers, its framework primarily considers temperature as a single variable and neglects the coupled effects of critical operating parameters such as pressure and current density. Subsequent studies addressing this limitation have refined parameterization methods by incorporating multi-physics coupling mechanisms, effectively improving the characterization of activation and concentration overpotentials. Existing ALK optimization efforts have predominantly targeted electrode materials, separator modification, and cell architecture to reduce overpotential and enhance single-stack efficiency [19–23], while largely overlooking the impact of balance-of-plant optimization on product purity. Absent is a holistic efficiency assessment of the entire system after integrating scrubbers, leaving industrial-scale plants without clear guidance for balancing purity compliance and energy consumption.

This study employs a semi-empirical modeling approach. Compared to the previous methods that used a single temperature variable for modeling, the model considers the influence of multi-variable coupling mechanisms such as temperature, current density and operating pressure on the characterization system of key performance indicators such as polarization characteristics, Faraday efficiency and product purity. Given that existing studies rarely conduct a comprehensive analysis and optimization of the entire water electrolysis system [24]. This study innovatively proposes a new electrolytic water hydrogen production system, and develops a model covering factory scale, combining thermodynamic equilibrium with multiphysics interactions to clarify the individual and synergistic effects of current density, operating pressure and temperature on hydrogen purity and the efficiency of the entire system, solving the neglected KOH gas entrainment problem in traditional alkaline water electrolysis. For the first time, it is revealed that there is an intersection of an efficiency characteristic curve between the purifier integrated system and the conventional system, and that the current density intersection tends to decay with increasing temperature. These findings provide a quantitative basis for optimizing industrial ALK units under the dual constraints of purity compliance and energy consumption.

It provides an important theoretical basis and practical guidance for the improvement and optimization of alkaline water electrolysis technology. The research results not only significantly improved the economy and environmental friendliness of alkaline electrolysis hydrogen production technology, but also provided a scalable methodological support for the engineering application of clean energy technology by establishing a system-level energy efficiency evaluation system.

2. System Configurations and Model Description

2.1. System configurations

Fig. 1(a) depicts the model architecture of a conventional alkaline water electrolysis (ALK) hydrogen production system developed using the Aspen Plus platform. The system incorporates four core modules: an electrolyzer unit, a dual-channel gas-liquid separation subsystem for hydrogen and oxygen streams, an electrolyte circulation loop, and a thermal management subsystem. The workflow is streamlined, with operational characteristics defined by a two-stage gas-liquid separation process. Mixed hydrogen-KOH and oxygen-KOH flows exiting the electrolyzer undergo primary separation in a gas-liquid separator, followed by direct entry into a secondary separator for further purification. A dedicated water replenishment pump integrated into the oxygen processing loop enables process water balance through targeted injection into the oxygen-side gas-liquid separator. Following separation, the hydrogen- and oxygen-end KOH streams are cooled *via* a heat exchanger and recirculated into the electrolyzer to maintain electrolyte homeostasis.

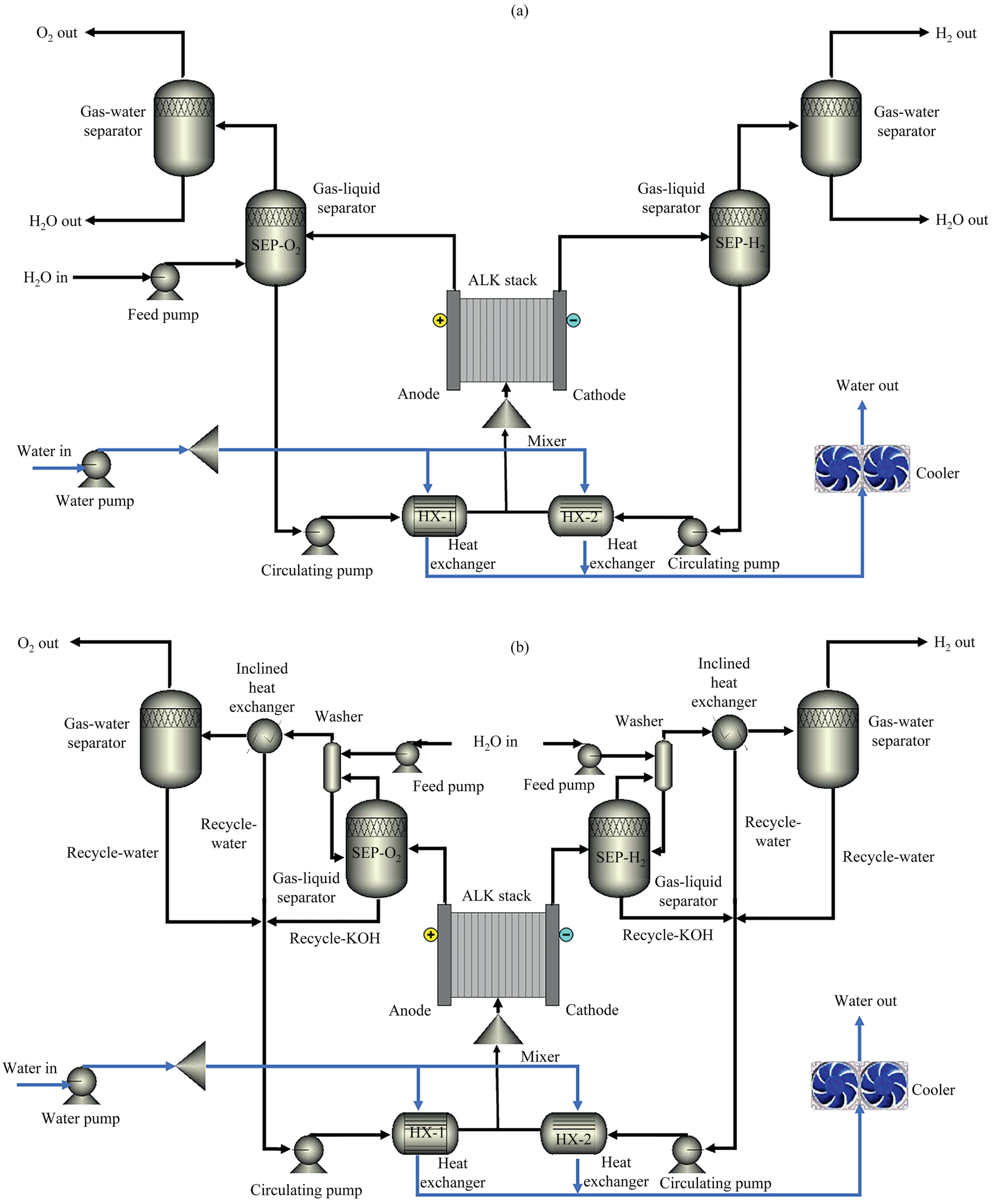

Fig. 1. (a) Traditional water electrolysis hydrogen production system and (b) integrated water electrolysis hydrogen production system.

Fig. 1(b) illustrates an enhanced ALK system incorporating an integrated scrubbing device. This system builds upon the conventional design by introducing a scrubbing column in the hydrogen purification pathway. The hydrogen-KOH mixture from the electrolyzer undergoes primary separation in the gas-liquid separator, but residual KOH droplets in the gas phase are captured *via* spray-deployed de-alkalizing water in the scrubbing column. This process performs three critical functions: entrained electrolyte particles are efficiently removed through impaction and coalescence, process water consumed during electrolysis is replenished, and the scrubbing liquid's latent heat exchange reduces the system's thermal load. The treated gas then proceeds to a secondary separator for deep dehydration, achieving hydrogen purity exceeding 99.5%. Condensate from the separator is gravity-fed back to the primary separator, forming a closed-loop water management system.

The oxygen processing channel mirrors the hydrogen pathway's design, with dual-channel pressure balancing maintaining the electrolyzer diaphragm's pressure differential within ±50 Pa, thereby preventing electrolyte cross-membrane permeation. Thermal-hydraulic optimization is further achieved through countercurrent heat exchange between the scrubber-discharged electrolyte and the feed alkali solution. The electrolyte circulation pump employs variable frequency control to dynamically adjust flow rates according to current density (0.1–0.4 $A\cdot cm^{-2}$), ensuring electrolyte concentration gradients remain within ±2% deviation. This integrated design synergizes scrubbing technology with multi-scale process control, enhancing both hydrogen purity and system efficiency while maintaining operational stability.

2.2. System model

2.2.1. Electrolyzer

The electrochemical model of the alkaline electrolyzer mainly predicts the electrochemical behavior of the electrolyzer under different operating conditions. The electrochemical-thermodynamic coupling modeling framework developed in the early stage [25,26] can determine the polarization curve, Faraday efficiency and gas purity according to the electrolyzer at different temperatures, pressures and current densities [27–30]. The polarization curve analyzes the potential under different operating conditions during the electrolysis process. Under the conditions of determined temperature and pressure, the potential of the electrolytic cell is determined according to the current density.

The cathode formula of the electrolysis reaction shown in Eq. (1):

$$4H^{+}(aq)+4e^{-}\rightarrow 2H_2(g) \tag{1}$$

The Anode formula of the electrolysis reaction shown in Eq. (2):

$$2H_2O(l)\rightarrow O_2(g)+4H^{+}(aq)+4e^{-} \tag{2}$$

Overall reaction shown in Eq. (3):

$$2H_2O(l)\rightarrow 2H_2(g)+O_2(g) \tag{3}$$

In order for the electrolysis reaction to occur, a minimum voltage is required, called the reversible voltage. This value decreases with increasing temperature. The reversible voltage under standard conditions (0.1 MPa and 25 °C) is 1.23 V.

The formula for the reversible voltage is shown in Eq. (4):

$$E_{\mathrm{rev}}(T)=1.50342-9.956\times 10^{-4}T+2.5\times 10^{-7}T^2 \tag{4}$$

The thermoneutral voltage is the actual energy requirement for electrolysis, meaning that some heat is required for water decomposition, as well as a minimum amount of voltage. At $T=298$ K, the thermoneutral voltage is 1.48 V, a value that does not vary much at different temperatures. Alkaline water electrolyzers typically operate between 1.8 and 2.4 V. Therefore, in most cases, such electrolyzers release heat during operation. The minimum voltage for water electrolysis under adiabatic conditions, when all the energy required for the electrochemical process is provided by electricity, is the thermoneutral cell voltage [31]. The voltage formula of the thermally neutral battery is shown in Eq. (5):

$$E_{\mathrm{tn}}=\frac{\Delta H}{2F} \tag{5}$$

However, under actual operating conditions, the battery voltage is always higher than the reversible voltage. This is because the activation overpotential, ohmic overpotential, and concentration gradient overpotential are caused by kinetic and resistance effects. In actual electrolysis reactions, the obstacles of reaction kinetics, electrolytic cell resistance, and concentration gradient need to be overcome. The actual battery voltage can be defined as the sum of the reversible voltage, activation overpotential, ohmic overpotential, and concentration gradient overpotential [27,32,33], as shown in Eq. (6):

$$V_{\mathrm{cell}}=V_{\mathrm{rev}}+(\widehat{\eta}_{\mathrm{cat}}+\widehat{\eta}_{\mathrm{an}}+\widehat{\eta}_{\mathrm{ohm}}+\widehat{\eta}_{\mathrm{conc}}) \tag{6}$$

Polarization curves can be determined using semi-empirical formulas. In this regard, one of the most widely used models is the one proposed by Uieberg [34]. The concentration overpotential has a greater effect at high current densities. Since AWE operates at relatively low current densities, the diffusion overpotential is not considered. It is not considered in Eq. (7):

$$V_{\mathrm{cell}}=V_{\mathrm{rev}}+[(r_1+d_1)+r_2\cdot T+d_2\cdot p]i+s\cdot \lg\left[\left(t_1+\frac{t_2}{T}+\frac{t_3}{T^2}\right)i+1\right] \tag{7}$$

Faraday efficiency refers to the ratio of the actual number of moles produced to the theoretical number of moles that should be produced in the same time [27], as shown in Eq. (8):

$$\eta_{\mathrm{F}}=\frac{n_{\mathrm{H2,prod}}}{n_{\mathrm{H2,th}}} \tag{8}$$

The Faraday efficiency can also be expressed as a function of temperature and current density, similar to the polarization curve [25]. Eq. (9) does not include pressure because it has little effect on the Faraday efficiency.

$$\eta_F=\left(\frac{i^2}{f_{11}+f_{12}\cdot T+i^2}\right)\cdot(f_{21}+f_{22}\cdot T) \tag{9}$$

All coefficients of the model are calculated by nonlinear regression.

Table 1
Coefficients considered for the electrochemical model of an alkaline water electrolysis cell.

Model	Coefficient	Value
Polarization curve	$r_1/\Omega\cdot m^2$	4.45153×10^{-5}
	$r_2/\Omega\cdot m^2\cdot{}^\circ C^{-1}$	6.88874×10^{-9}
	$d_1/\Omega\cdot m^2$	-3.12996×10^{-6}
	$d_2/\Omega\cdot m^2\cdot bar^{-1}$	4.47137×10^{-7}
	s/V	0.33824
	$t_1/m^2\cdot A^{-1}$	−0.01539
	$t_2/m^2\cdot{}^\circ C\cdot A^{-1}$	2.00181
	$t_3/m^2\cdot{}^\circ C^2\cdot A^{-1}$	15.24178
Faraday efficiency	$f_{11}/A^2\cdot m^{-4}$	478645.74
	$f_{12}/A^2\cdot m^{-4}\cdot{}^\circ C^{-1}$	−2953.15
	f_{21}	1.03960
	$f_{22}/{}^\circ C^{-1}$	−0.00104
Gas purity (hydrogen in oxygen)	C_1	0.09901
	$C_2/{}^\circ C^{-1}$	−0.00207
	$C_3/{}^\circ C^{-2}$	1.31064×10^{-5}
	C_4	−0.08483
	$C_5/{}^\circ C^{-1}$	0.00179
	$C_6/{}^\circ C^{-2}$	-1.13390×10^{-5}
	$C_7/A\cdot m^{-2}$	1481.45
	$C_8/A\cdot m^{-2}\cdot{}^\circ C^{-1}$	−23.60345
	$C_9/A\cdot m^{-2}\cdot{}^\circ C^{-2}$	−0.25774
	E_1	3.71417
	E_2/bar^{-1}	−0.93063
	E_3/bar^{-2}	0.05817
	E_4	−3.72068
	E_5/bar^{-1}	0.93219
	E_6/bar^{-2}	−0.05826
	$E_7/A\cdot m^{-2}$	−18.38215
	$E_8/A\cdot m^{-2}\cdot bar^{-2}$	5.87316
	$E_9/A\cdot m^{-2}\cdot bar^{-2}$	−0.46425

Note: 1 bar = 0.1 MPa.

Table 1 shows the values of the parameters.

Heat release is shown in Eq. (10):

$$Q_{\mathrm{gen}} = N \cdot I \cdot (V_{\mathrm{cell}} - V_{\mathrm{tn}}) \tag{10}$$

The excess heat causes the temperature of the electrolyte flow and the gases produced in the battery stack to rise. Therefore, it must be continuously removed to ensure a constant operating temperature.

The electricity consumed by the electrolytic cell is shown in Eq. (11):

$$W = V_{\mathrm{cell}} \cdot N \cdot i_{\mathrm{cell}} \cdot A_{\mathrm{cell}} \tag{11}$$

where V_{cell} is the cell voltage of the electrolytic cell; N is the number of electrolytic cell cells; i_{cell} is the current density; A_{cell} is the cell area.

Mass balance:

The hydrogen production rate at the cathode depends on the electrochemical behavior of the cell and can be determined using the Faradaic efficiency *via* Eq. (12)–Eq. (16).

$$n_{\mathrm{H_2,prod}} = \eta_{\mathrm{F}} \frac{I}{zF} N \tag{12}$$

$$n_{\mathrm{O_2,an}} = n_{\mathrm{O_2,prod}} = \frac{1}{2} n_{\mathrm{H_2,prod}} \tag{13}$$

$$n_{\mathrm{H_2O}} = n_{\mathrm{H_2,prod}} \tag{14}$$

$$n_{\mathrm{H_2,cat}} = n_{\mathrm{H_2,prod}} \tag{15}$$

$$n_{\mathrm{H_2,an}} = n_{\mathrm{HTO}} \tag{16}$$

2.2.2. Separator

The hydrogen and oxygen produced by electrolysis in the electrolyzer will be mixed with the electrolyte and discharged through the pipeline. A separation device is required to separate the final product hydrogen from the electrolyte. The mass balance is established based on the variable separation efficiency parameter of the system. The mass balance of the hydrogen-electrolyte separation container can be expressed as:

$$\sum \mathrm{mf}_i = \mathrm{mf}_{\mathrm{H_2},i} + \mathrm{mf}_{\mathrm{ele},i} + \mathrm{mf}_{\mathrm{m},i} \tag{17}$$

$$\sum \mathrm{mf}_j = \left[\mathrm{mf}_{\mathrm{H_2},i} n_{\mathrm{s}} + \mathrm{mf}_{\mathrm{ele},i}(1 - n_{\mathrm{sl}})\right] + \left[\mathrm{mf}_{\mathrm{ele},i} n_{\mathrm{sl}} + \mathrm{mf}_{\mathrm{H_2},i}(1 - n_{\mathrm{s}}) + \mathrm{mf}_{\mathrm{m},i}\right] \tag{18}$$

where the total inlet mass flow mf_i, kg·h^{-1}, as seen in Eq. (17), is calculated as the sum of the hydrogen flow produced in weight mass plus the mass flow rate of electrolyte $\mathrm{mf}_{\mathrm{ele},i}$, kg·h^{-1}, and the mass flow rate of the make-up feed water $\mathrm{mf}_{\mathrm{m},i}$, kg·h^{-1}. On the other hand, as shown in Eq. (18), the total outlet mass flow rate mf_j, kg·h^{-1}, can be divided into two parts. In the first part of the equation, the flow rate out of the upper outlet of the container is estimated based on the gas and liquid separation efficiencies n_{s} and n_{sl}. This flow rate is a mixed flow of hydrogen bubbles and the impure electrolyte part that is dragged upward in the form of moisture. In the second part of the equation, the flow rate out of the lower part of the container is calculated, also based on the separation efficiency. This flow rate is a mixed flow of electrolyte that flows back to the electrolyzer stack and the hydrogen impurity part that is dragged downward in the circulating electrolyte loop.

The separator is modeled and designed using an adiabatic isothermal model, where heat loss to the surrounding environment is negligible and the inlet temperature is equal to the temperature of the gas phase outlet and the liquid phase outlet.

2.2.3. Heat exchanger

The mass flow rate of the stream remains constant when entering and leaving the heat exchanger, because the heat exchanger does not change the amount of the stream, only its energy state. The mass balance equation of the heat exchanger can be expressed as Eq. (19):

$$\sum_{i=1}^{n} m_{i,\mathrm{in}} = \sum_{j=1}^{m} m_{j,\mathrm{out}} \tag{19}$$

where $m_{i,\mathrm{in}}$ represents the mass flow rate of the *i-t*h stream entering the heat exchanger, kg·h^{-1}, $m_{j,\mathrm{out}}$ represents the mass flow rate of the *j*-th stream leaving the heat exchanger, kg·h^{-1}, n is the number of streams entering the heat exchanger, and m is the number of streams leaving the heat exchanger, kg·h^{-1}.

This equation ensures that the total mass flow rate entering the heat exchanger is equal to the total mass flow rate leaving the heat exchanger.

The modeling of the condenser aims to achieve cooling of the gas-liquid mixed stream to a predetermined temperature. There are many types of condensers. The one used in this work is based on the shell and tube condenser. Cooling water is used to cool the gas-liquid mixed stream. Since the target temperature is known, Aspen Plus uses the fluid inflow to estimate the heat removed from the condenser. The energy formula is shown as Eq. (20):

$$Q = mC_{p,\mathrm{avg}} \Delta T \tag{20}$$

where Q is the rate of heat removed, kJ·h^{-1}, m is the mass flow rate of the gas-liquid mixture, kg·h^{-1}, and ΔT is the change in inlet and outlet temperature. $C_{p,\mathrm{avg}}$ is the average specific heat capacity of the gas-liquid mixture.

The shell and tube heat exchanger used in this work is modeled at steady state using the logarithmic mean temperature difference (LMTD) method to resolve its thermo-fluid performance. This method is applicable in this case because the target temperature is known. The LMTD method is described in detail by Kay and Nedderman. It is generally defined by the following Eq. (21):

$$Q = (UA)\Delta T_{\mathrm{ln}} \tag{21}$$

where Q is the heat load, ΔT_{ln} Tis the logarithmic mean temperature difference LMTD between the hot end (subscript, h) and the cold end (subscript, c) of the heat exchanger, as shown in Eq. (22):

$$\Delta T_{\mathrm{ln}} = \frac{\left(T_{\mathrm{h,i}} - T_{\mathrm{c,o}}\right) - \left(T_{\mathrm{h,o}} - T_{\mathrm{c,i}}\right)}{\ln\left[\dfrac{\left(T_{\mathrm{h,i}} - T_{\mathrm{c,o}}\right)}{\left(T_{\mathrm{h,o}} - T_{\mathrm{c,i}}\right)}\right]} \tag{22}$$

The subscripts i and o represent inlet and outlet respectively.

2.2.4. Pumps

The mass balance equation of the pump follows the law of conservation of mass, and its mass balance equation can be simplified to the total mass flow rate of the input flow equal to the mass flow rate of the output flow. The mass balance equation can be expressed as Eq. (23):

$$m_{\mathrm{in}} = m_{\mathrm{out}} \tag{23}$$

where m_{in} is the mass flow rate of the flow at the pump inlet, $\mathrm{kg \cdot h^{-1}}$, and m_{out} is the mass flow rate of the flow at the pump outlet, $\mathrm{kg \cdot h^{-1}}$.

In the system, the pump is mainly used to increase the pressure of the fluid to the required value. The power required to increase the pressure is calculated. To avoid cavitation in the fluid pump, the pump is generally used to process a single liquid phase or a gas-liquid mixed fluid containing a small amount of gas. The centrifugal pump is modeled based on the pressure difference between the outlet and the inlet under predefined adiabatic and isentropic efficiencies to determine the power loss of the pump. The power is given by the following formula.

The power consumption process of the working fluid pump is shown in Eq. (24) as follows:

$$W_{\mathrm{p}} = m(h_2 - h_1) = \frac{m(h_{2s} - h_1)}{\eta_{\mathrm{p}}} \tag{24}$$

where m is the mass of the working fluid, $\mathrm{kg \cdot h^{-1}}$; h is the enthalpy value of the working fluid at each state point, $\mathrm{kJ \cdot kg^{-1}}$; W_{p} is the power consumption of the working fluid pump, kW; η_{p} is the mechanical efficiency of the working fluid pump; h_{2s} represents the ideal process enthalpy value at this state point.

2.3. Model validation

For simulation validation, the data from the test bench in the published paper were used. The bench can produce 2.5 $\mathrm{m^3 \cdot h^{-1}}$ of hydrogen [25]. The experimental system is configured as follows: the electrolyzer consists of 12 bipolar electrolysis units with an effective reaction area of 1000 $\mathrm{cm^2}$, the energy supply system is equipped with a dual-channel programmable DC power supply, and the online mass spectrometer monitors the purity of the product gas in real time. The platform operating parameters cover the typical industrial operating range of temperature 40–80 °C and pressure 1–10 bar (1 bar = 0.1 MPa), and multi-parameter coordinated control is achieved through a PLC-based distributed control system. The experimental data obtained in this test bench have been used to calculate the coefficients shown in Table 1.

3. Results and Discussion

This study built a steady-state simulation framework based on the Aspen Plus platform. In order to calculate the output under different working conditions, the required data were introduced into the model. As shown in Table 2, the input parameters of the benchmark condition strictly follow the typical operating data of the industrial alkaline electrolyzer. Similarly, the following assumptions are considered to simplify the simulation process.

Table 2
Input data for the system simulation at base-case operation conditions (75 °C and 0.7 MPa).

Parameter	Value
Stack working temperature, T_{stack}/°C	75
Operating system pressure, P_{stack}/MPa	0.7
Electrolyte concentration (KOH)/% (mass)	35
Active electrode area, $A_{\mathrm{cell}}/\mathrm{cm^2}$	1000
Cell number, N/cells	12
Input power stack, W_{stack}/kW	10

All processes are operating at steady state.

All gases in the system behave like ideal gases.

The deionized water input to the system is at 298 K.

The AEL stack is operated at balanced anode and cathode pressures.

3.1. Effects of current density and temperature on water conversion efficiency and electrical power

In this study, the feed conditions of the electrolysis system were set as follows: the inlet flow was 900 $\mathrm{kg \cdot h^{-1}}$, and the mass fraction of potassium hydroxide was 35%. Fig. 2(a) shows the influence of current density (0.1–0.4 $\mathrm{A \cdot cm^{-2}}$) and electrolysis temperature (40–80 °C) on the water decomposition conversion rate. The results show that under constant temperature conditions, the water conversion rate increases with the increase of current density. Increasing the current density can promote the occurrence of water decomposition reaction, resulting in more water conversion to H_2 and O_2. Increasing the current density means that the amount of charge passing through the electrode surface per unit time increases, which means that more electrons can participate in the reaction at the same time, thereby accelerating the rate at which water molecules decompose into hydrogen and oxygen. The increase in temperature leads to a decrease in water conversion rate. This phenomenon is directly related to the increase in parasitic current loss and the decrease in Faraday efficiency caused by the increase in temperature. When the electrolyzer is operated at 40 °C and the current density is 0.4 $\mathrm{A \cdot cm^{-2}}$, the maximum water conversion rate is 0.269%.

Fig. 2(b) reveals the coupling mechanism of current density (0.1–0.4 $\mathrm{A \cdot cm^{-2}}$) and electrolysis temperature (40–80 °C) on the power demand of the electrolysis system. Experimental data show that the electrolysis power and current density show a significant positive correlation, which is due to the increase in ohmic overpotential and polarization overpotential caused by the increase in current density, resulting in an increase in electrolysis voltage. In the temperature dimension, the electrolysis power shows a negative correlation with the increase in temperature under specific current density conditions. This phenomenon is directly related to the decrease in activation overpotential caused by the increase in temperature, which in turn reduces the working voltage of the electrolyzer. When the electrolyzer is operated at 40 °C and the current density is 0.4 $\mathrm{A \cdot cm^{-2}}$, the maximum power required is 15174 W. When the operating condition is 80 °C and the current density is 0.1 $\mathrm{A \cdot cm^{-2}}$, the minimum power required is 2571 W.

3.2. Effects of gas-liquid entrainment and stream temperature on scrubbers

This study aims at the KOH micro-droplet entrainment phenomenon at the gas phase outlet of the gas-liquid separator of the industrial alkaline water electrolysis system, and studies the KOH entrainment purification mechanism through an integrated scrubber. Fig. 3(a), (b) reveals the effect of gas-liquid entrainment concentration and stream temperature on the mass flow rate of water at the gas phase outlet of the scrubber. The results show that the hydrogen and oxygen double-end scrubbers present similar mass migration characteristics:

With the increase of gas-liquid entrainment, the mass flow rate of water at the gas phase outlet of the hydrogen end scrubber also increases. However, this growth shows nonlinear characteristics. Specifically, at lower gas-liquid entrainment values, the increase in mass flow is more significant; while at higher entrainment values,

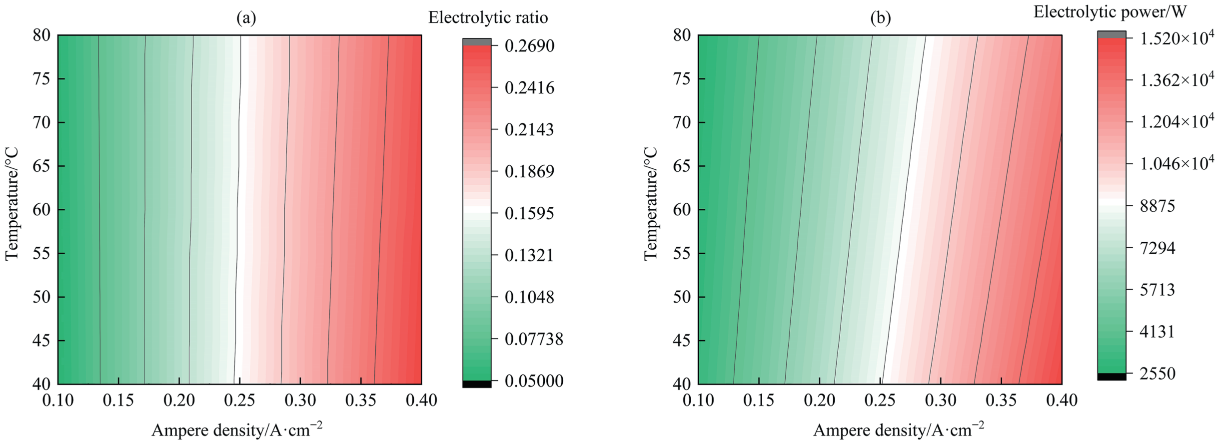

Fig. 2. (a) Effect of current density and temperature on water conversion efficiency, (b) effect of current density and temperature on required electrical power.

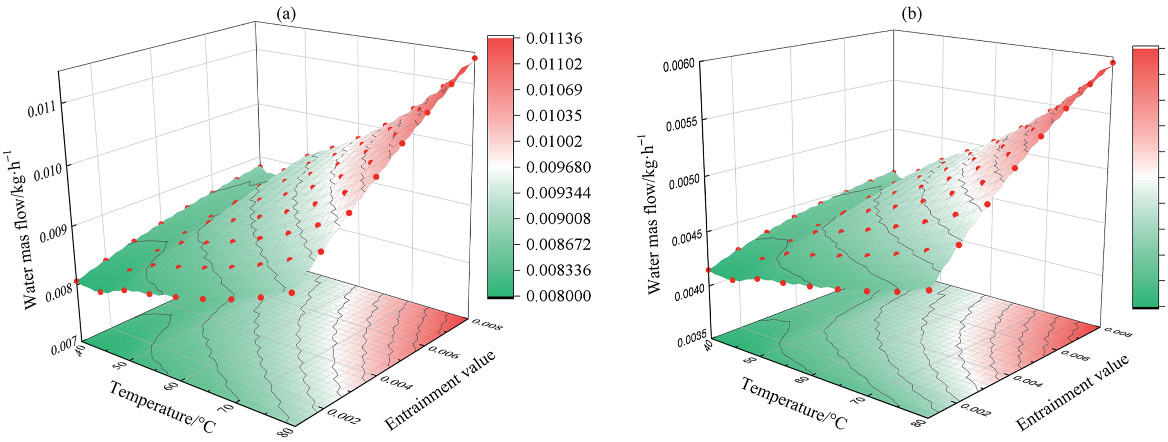

Fig. 3. (a) Effect of gas liquid entrain and temperature at hydrogen end on mass flow of water at gas phase outlet of scrubber, (b) effect of gas liquid entrain and temperature at oxygen end on mass flow of water at gas phase outlet of scrubber.

the growth rate of mass flow slows down. The entrainment contains KOH aqueous solution. The higher the entrainment amount, the phenomenon is related to the decrease in aerosol capture efficiency caused by the inertial dissipation effect of KOH droplets.

With the increase of temperature, the mass flow rate at the hydrogen end shows a trend of gradual increase. As the temperature increases, the saturated vapor pressure of water increases, allowing more water molecules to transform from liquid phase to gas phase, thereby increasing the mass flow rate of water at the hydrogen end and oxygen end.

The simulation data show that the removal efficiency of KOH by the scrubber is always maintained above 99.98%, indicating that the integrated scrubbing device can effectively deal with the KOH entrainment problem that occurs in actual industrial production.

3.3. *Effects of pressure and temperature on gas-liquid separators*

This study reveals the effect of operating pressure (0.7–0.9 MPa) and temperature (40–80 °C) on the purity of hydrogen in the primary gas-liquid separator through Fig. 4(a). The data show that under fixed pressure conditions, the mole fraction of hydrogen shows a systematic downward trend with increasing temperature. Every 5 °C increase in temperature leads to a decrease in hydrogen purity of 0.08%–0.46% points. This phenomenon is directly related to the increase in water vapor partial pressure caused by the increase in temperature. As the partial pressure of water vapor increases, the water vapor content in the gas phase of the system increases, resulting in a decrease in the molar fraction of hydrogen. Under constant temperature conditions, an increase in operating pressure (0.7 → 0.9 MPa) can increase the purity of hydrogen by 0.05%–0.5% points. This is due to the inhibitory effect of increased pressure on the gas phase liquid holdup, which leads to an increase in the molar fraction of hydrogen in the gas phase.

Fig. 4(b) shows the regulation of hydrogen purity by the operating pressure (0.7–0.9 MPa) and temperature (40–80 °C) in the secondary gas-liquid separator after cooling by the heat exchanger. The data show that in the secondary separation stage, the hydrogen mole fraction is stably maintained at 99.54% ± 0.04%, showing the following characteristics: (1) Temperature changes have no significant effect on gas phase purity, which is due to the fact that after cooling water is collected by the inclined heat exchanger, the water content in the gas phase has dropped below the dew point temperature of the separator; (2) Every 0.02 MPa increase in pressure only slightly increases the hydrogen purity by 0.007%–0.01% points. This phenomenon is related to the strong non-ideal characteristics of the gas-liquid equilibrium curve - when the gas phase water concentration is lower than 200 $\mu L\cdot L^{-1}$, the regulation of pressure on the gaseous water content is limited by thermodynamics. The secondary separator mainly undertakes the function of deep dehydration, and its performance is related to the cooling effect of the previous heat exchanger unit.

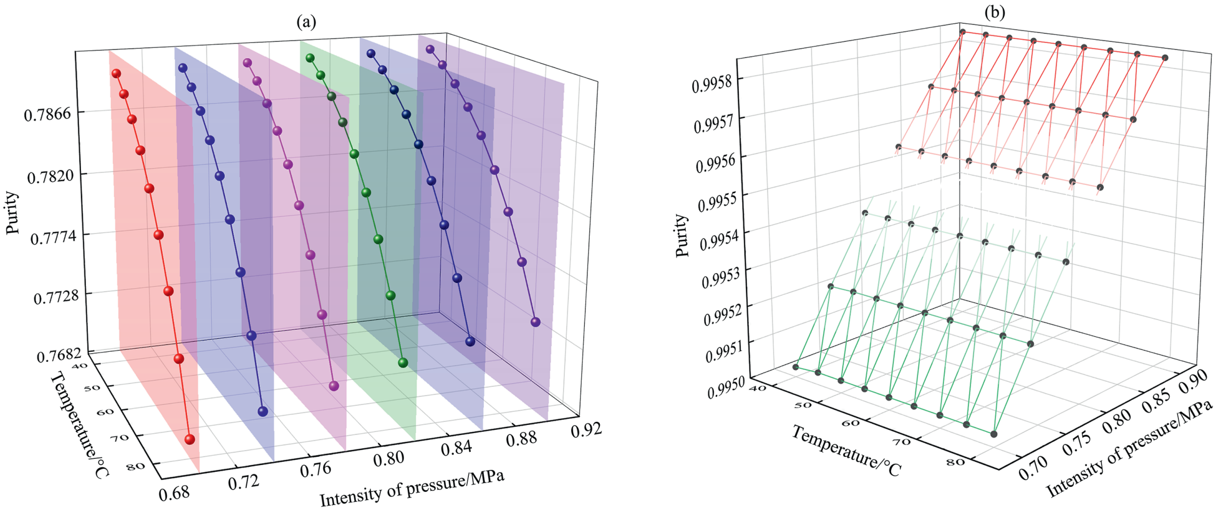

Fig. 4. (a) Effect of pressure and temperature on hydrogen purity of the primary gas-liquid separator, (b) effect of pressure and temperature on hydrogen purity in the secondary.

3.4. Effects of inlet stream pressure and heat exchanger temperature on the integrated system

Based on the Aspen Plus process simulation platform, the influence mechanism of multiple parameters such as current density (0.1–10.4 A·cm^{-2}), inlet temperature (40–80 °C), operating pressure (0.7–0.9 MPa) and heat exchanger temperature (25–40 °C) on system efficiency and product hydrogen purity was explored. The simulation data in Fig. 5(a), (b) reveal the following key rules:

Under typical operating conditions (0.15 A·cm^{-2}, 80 °C), when the inlet stream pressure is maintained at 7 bar, when the heat exchanger temperature rises from 25 °C to 40 °C, the system efficiency increases by 0.012% points (41.627%→41.639%), and the hydrogen purity decreases by 0.65% points (99.50%→98.85%), which is related to the attenuation of gas-liquid separation efficiency caused by the increase in the inlet temperature of the secondary flash tank. When the heat exchanger temperature is maintained at 25 °C, the operating pressure is increased from 0.7 MPa to 0.9 MPa, and the hydrogen purity increases by 0.09% points (99.50%→99.59%), which is attributed to the improvement of the flash tank separation efficiency under high-pressure conditions; the system efficiency decreases by 0.2% points (41.63%→41.43%).

The operating condition analysis shows that when the inlet pressure is 0.9 MPa and the heat exchanger temperature is 25 °C, the maximum H_2 concentration is 99.6%; when the inlet pressure is 0.7 MPa and the heat exchanger temperature is 40 °C, the system efficiency is the highest, which is 41.63%.

3.5. Effects of current density and temperature on the integrated system

An analysis was conducted on an industrial-grade gas-liquid separation system (product H_2 purity ≥99.5%), focusing on revealing the regulation mechanism of current density (0.1–0.4 A·cm^{-2}) and inlet temperature (40–80 °C) on the system efficiency peak. As shown in Fig. 6(a), under the purity constraint condition: when the current density increases, the polarization voltage increases, the power required by the electrolyzer increases, which increases the input power of the system. At the same time, the conversion rate of H_2O also increases, which means that the chemical energy output by the system also increases. Under typical working conditions (0.7 MPa, 80 °C), in the low current density area (0.1–0.2 A·cm^{-2}), the efficiency of the system shows an increasing trend, and the efficiency improvement rate reaches 26.7%. In this stage, the increase in

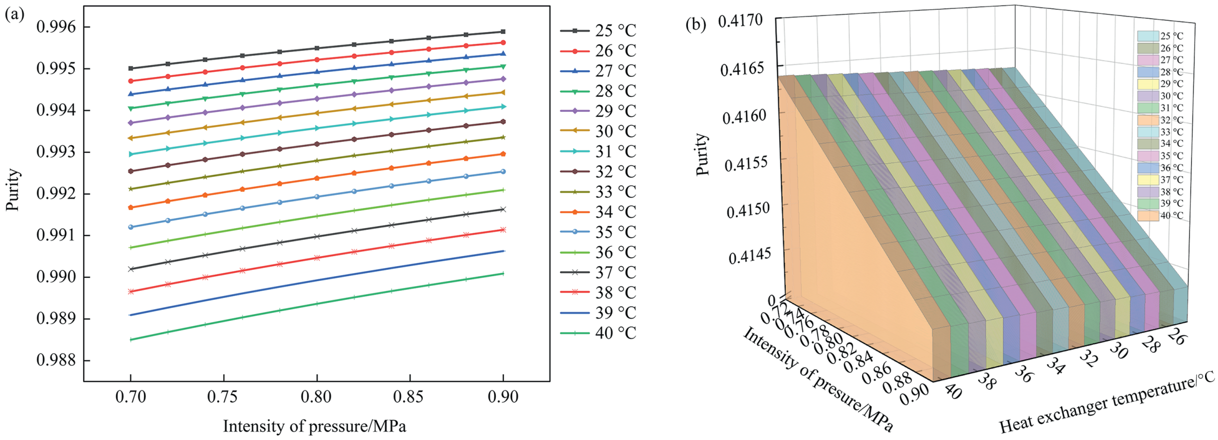

Fig. 5. (a) Effect of inlet stream pressure and heat exchanger temperature on system outlet H_2 concentration, (b) effect of inlet stream pressure and heat exchanger temperature on system efficiency.

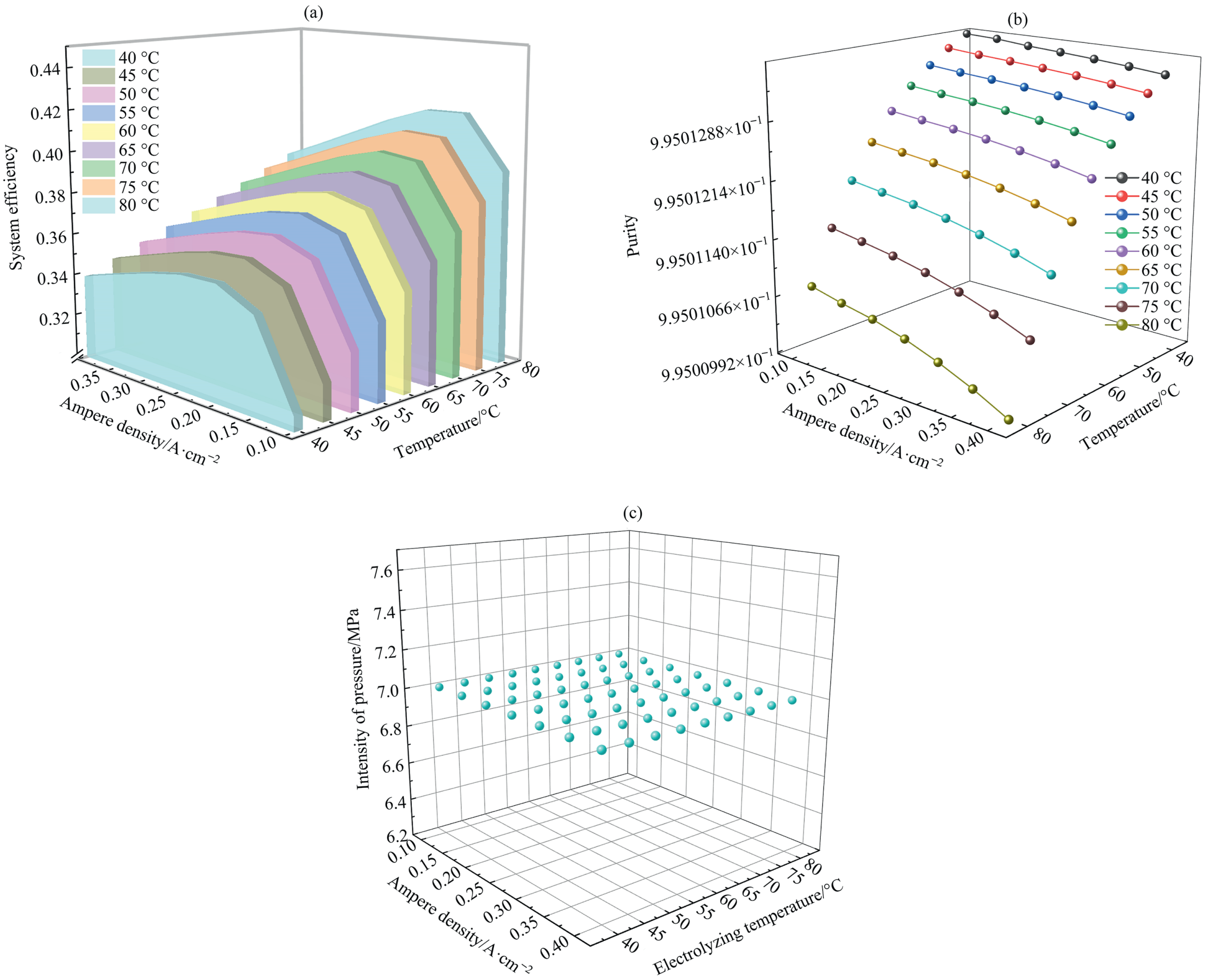

Fig. 6. (a) Effect of current density and temperature on maximum system efficiency, (b) H_2 concentration at outlet when maximum system efficiency is achieved at different current density and temperature, (c) electrolysis pressure at different current density and temperature to achieve maximum system efficiency.

water decomposition conversion rate is dominant, and the increase in chemical energy output by the system is greater than the increase in electrical energy input by the system; while in the high current density area (>0.2 $A\cdot cm^{-2}$), the increase in chemical energy output by the system is less than the increase in electrical energy input by the system. At this time, the efficiency of the system shows a decreasing trend, and the efficiency decrease rate reaches 16.17%.

The efficiency shows an increasing trend with the increase in temperature. Under typical working conditions (0.15 $A\cdot cm^{-2}$, 0.7 MPa), the efficiency can be increased by an average of 1.6% points for every 10 °C increase in temperature. This phenomenon is due to the fact that the inhibitory effect of temperature on the activation overpotential exceeds its negative impact on the reduction of Faraday efficiency, resulting in the reduction of the chemical energy output of the system being lower than the reduction of the electrical energy input to the system. The net effect is an increase in the energy conversion rate.

Fig. 6(b) analyzes the outlet H_2 concentration when the maximum system efficiency is achieved at different current densities and temperatures. The increase in current density reduces the H_2 concentration, and the increase in temperature reduces the H_2 concentration. However, in terms of quantity, this effect is very small, and the difference between the maximum and minimum values does not exceed 0.0004%. This effect can be ignored. Fundamentally speaking, the decisive factors affecting the H_2 concentration are still the temperature and pressure of the gas-liquid separator inlet stream.

Fig. 6(c) shows the electrolysis pressure at different current density and temperature to achieve maximum system efficiency. Based on the above rules, the optimal operating parameter combination is determined as: current density 0.15 $A\cdot cm^{-2}$, operating pressure 0.7 MPa, electrolysis temperature 80 °C, heat exchanger outlet temperature 25 °C. Under this configuration, the system achieves a peak efficiency of 41.6286% and meets the industrial-grade hydrogen purity standard. This parameter stability feature provides important theoretical support for the robustness control of alkaline electrolysis systems under renewable energy fluctuation scenarios.

3.6. *The impact of temperature and pressure on the traditional system*

This study revealed the variation of system efficiency and hydrogen purity through parameter sensitivity analysis (Fig. 7). When the current density varies between 0.1 and 0.4 $A\cdot cm^{-2}$, the system efficiency and H_2 concentration vary in the same way as the electrolysis temperature and electrolysis pressure. Under

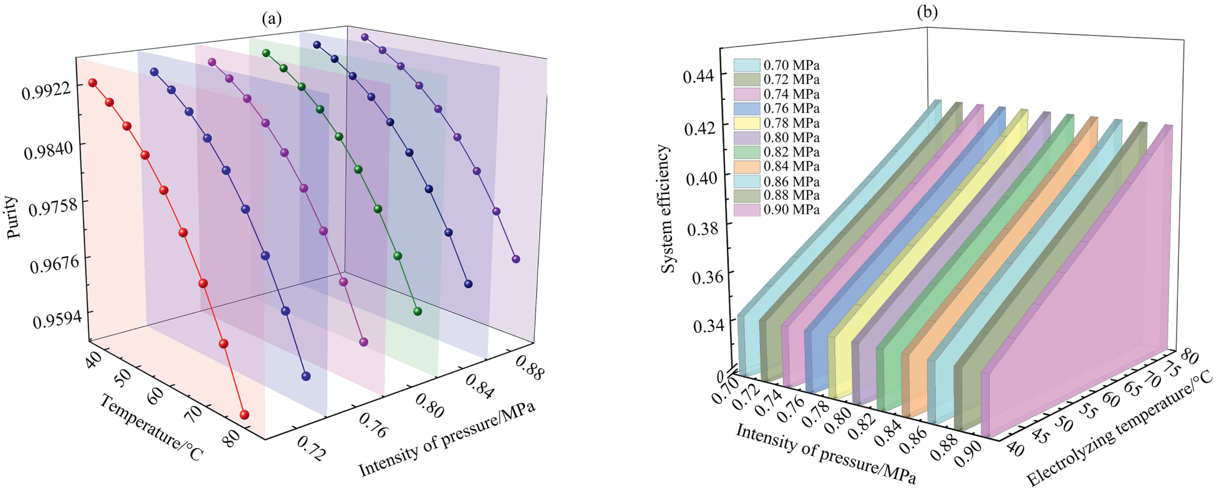

Fig. 7. Effect of changes in electrolysis temperature and electrolysis pressure on system efficiency and H_2 concentration.

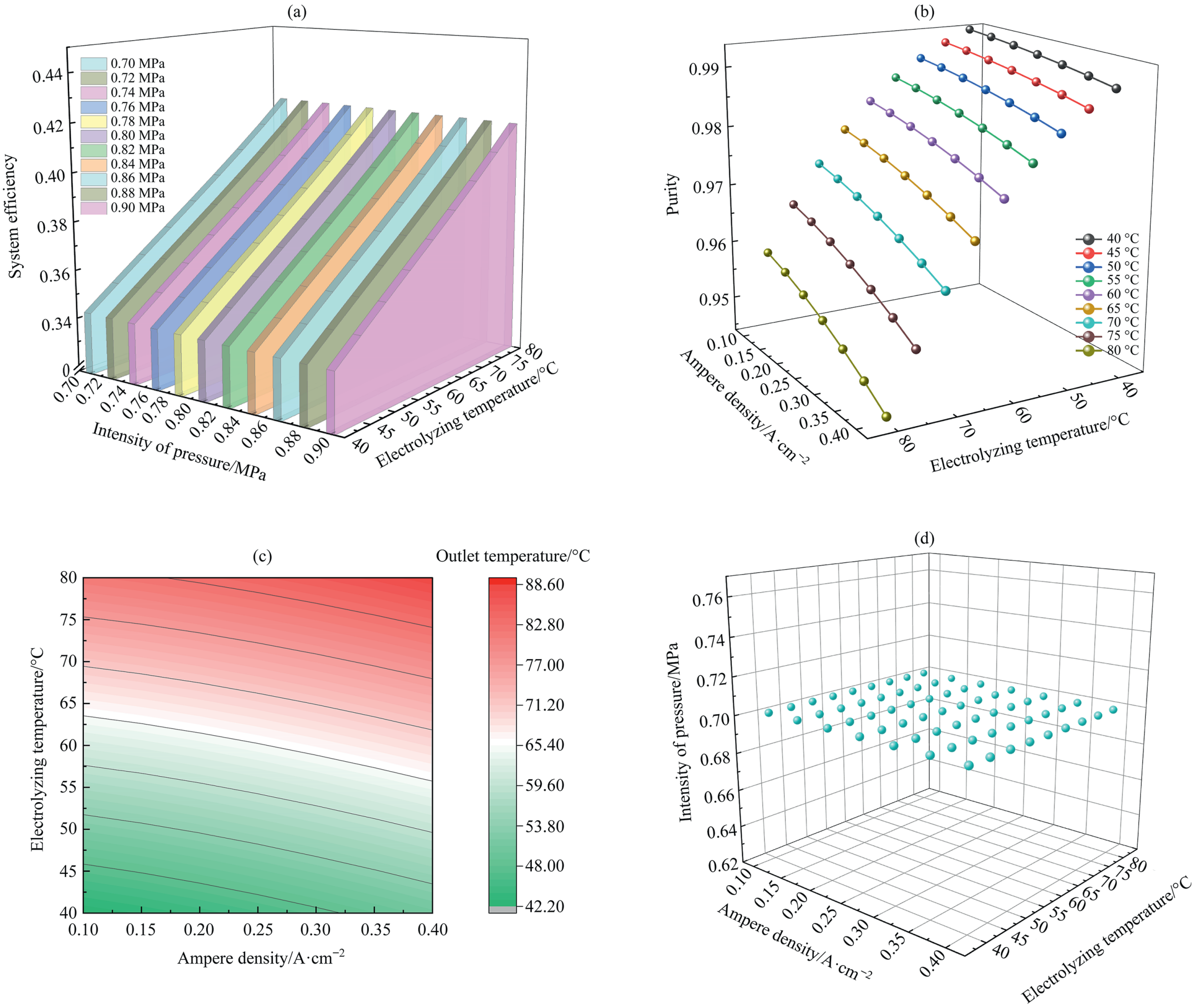

Fig. 8. (a) Effect of electrolysis temperature and current density on system efficiency, (b) effect of electrolysis temperature and current density on outlet H_2 concentration, (c) the outlet temperature of the electrolytic cell at different electrolysis temperatures and current densities, (d) electrolysis pressure at different current densities and temperatures to achieve maximum system efficiency.

constant current density (0.3 A·cm^{-2}), the system performance exhibits the following characteristics:

As the electrolysis temperature increases, the H_2 concentration decreases, and as the electrolysis pressure decreases, the H_2 concentration decreases. The reason is that the changes in electrolysis temperature and pressure cause the temperature and pressure of the secondary flash inlet stream to change in the same way, so the trend of H_2 concentration changing with electrolysis temperature and pressure is the same as the trend of H_2 concentration changing with the temperature and pressure of the secondary flash inlet stream.

As the electrolysis temperature increases, the system efficiency increases, the conversion rate of H_2O decreases, the chemical energy of hydrogen generated by the system decreases, the input power of the electrolyzer decreases, and the energy consumption of the heat exchanger and water pump decreases. Overall, the reduction in the chemical energy output of the system is lower than the reduction in the input electrical energy of the system, and the system efficiency increases.

3.7. *Effects of temperature and current density on the traditional system*

Under certain electrolysis temperature and electrolysis pressure, the system efficiency and H_2 concentration show the same trend as the current density changes, as shown in the figure.

As shown in Fig. 8(a), the maximum efficiency of the system changes at different current densities and electrolysis temperatures, as well as the corresponding pressure and H_2 concentration when the system is at maximum efficiency, are explored. The maximum efficiency of the system shows a trend of first increasing and then decreasing with the increase of current density, and shows an increasing trend with the increase of temperature. The reason analysis is the same as that of integrated systems.

Fig. 8(b) analyzes the effect of electrolysis temperature and current density on outlet H_2 concentration. The increase of current density reduces the H_2 concentration, and the increase of temperature reduces the H_2 concentration. As shown in Fig. 8(c), the increase of current density leads to the increase of inlet stream temperature of the primary and secondary flash tanks. The mechanism of increasing current density to reduce H_2 concentration is the same as that of increasing temperature to reduce H_2 concentration. As the temperature increases, more water molecules evaporate from the solution, resulting in a corresponding decrease in the proportion of hydrogen.

Through multi-condition optimization analysis, it was determined that within the wide range of electrolysis temperature (40–80 °C) and current density (0.1–0.4 A·cm^{-2}), As shown in Fig. 8(d), the optimal operating pressure for achieving maximum system efficiency is stably maintained at 0.7 MPa. Based on this, the peak efficiency operating condition parameter combination is established as: current density 0.15 A·cm^{-2}, operating pressure 0.7 MPa, electrolysis temperature 80 °C. Experimental data show that under this configuration, the system energy conversion efficiency reaches 41.66%, and the product hydrogen concentration is 95.68%.

3.8. *System efficiency comparison*

By comparing and analyzing the energy efficiency-purity characteristics of the dual systems under the 7 bar reference pressure (Table 3), the influence of the system architecture on the adaptability to working conditions is revealed.

There is a significant crossover phenomenon in the efficiency characteristic curves of the two systems, As shown in Fig. 9, under the reference pressure of 7 bar, the current density

Table 3
Energy efficiency of the dual systems under different temperature and current density.

	1000 A·m^{-2}	1500 A·m^{-2}	2000 A·m^{-2}	2500 A·m^{-2}	3000 A·m^{-2}	3500 A·m^{-2}	4000 A·m^{-2}
System efficiency at electrolysis temperature of 40 °C							
Integrated systems	0.30414	0.3433	0.35246	0.35202	0.34823	0.34328	0.33801
Traditional systems	0.30378	0.34309	0.35236	0.35197	0.34823	0.34331	0.33807
System efficiency at electrolysis temperature of 45 °C							
Integrated systems	0.31437	0.35235	0.3605	0.3593	0.35494	0.34955	0.34391
Traditional systems	0.31403	0.35216	0.36043	0.3593	0.35498	0.34962	0.34402
System efficiency at electrolysis temperature of 50 °C							
Integrated systems	0.32452	0.36119	0.36827	0.36631	0.36137	0.35552	0.34952
Traditional systems	0.3242	0.36106	0.36822	0.36634	0.36146	0.35564	0.34967
System efficiency at electrolysis temperature of 55 °C							
Integrated systems	0.33473	0.36995	0.37591	0.37314	0.36762	0.36131	0.35495
Traditional systems	0.33442	0.36985	0.37593	0.37323	0.36776	0.36149	0.35516
System efficiency at electrolysis temperature of 60 °C							
Integrated systems	0.3451	0.37873	0.3835	0.37992	0.37379	0.36703	0.36028
Traditional systems	0.34483	0.37868	0.38359	0.38008	0.374	0.36727	0.36056
System efficiency at electrolysis temperature of 65 °C							
Integrated systems	0.35577	0.38764	0.39116	0.38673	0.37999	0.37275	0.36563
Traditional systems	0.35554	0.38766	0.39132	0.38697	0.38028	0.37307	0.36598
System efficiency at electrolysis temperature of 70 °C							
Integrated systems	0.36682	0.39679	0.399	0.39368	0.3863	0.37857	0.37106
Traditional systems	0.36664	0.39689	0.39924	0.394	0.38668	0.37899	0.37151
System efficiency at electrolysis temperature of 75 °C							
Integrated systems	0.37839	0.40629	0.40713	0.40088	0.39283	0.38459	0.37667
Traditional systems	0.37829	0.40649	0.40747	0.40131	0.39332	0.38512	0.37722
System efficiency at electrolysis temperature of 80 °C							
Integrated systems	0.39063	0.41629	0.41566	0.40851	0.39968	0.3909	0.38255
Traditional systems	0.39063	0.41661	0.41614	0.409	0.4003	0.39156	0.38323

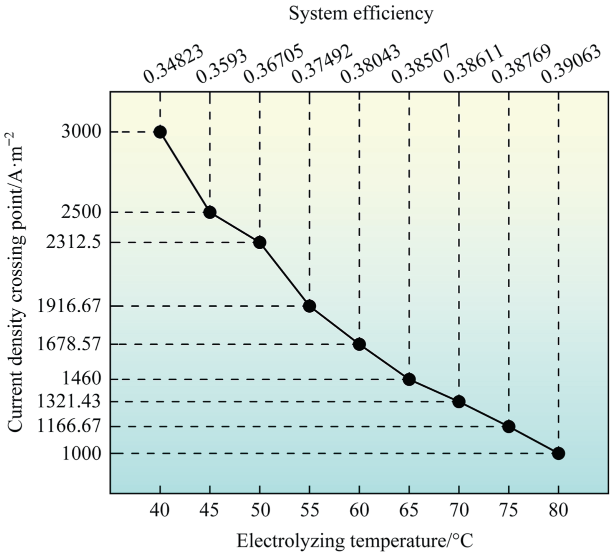

Fig. 9. The variation trend of current density intersections with temperature.

crossover point (i_c) tend to decrease with the increase of electrolytic temperature. when the temperature rises from 40 °C to 80 °C, The current density crossover point (i_c) has increaased from 1000 A·m^{-2} to 3000 A·m^{-2}, with a growth rate of 50 A·(m^2·°C)$^{-1}$. This critical point divides the operating domain into two characteristic areas: low current area ($i < i_c$): integrated systems has a significant efficiency advantage; high current area ($i < i_c$): traditional systems shows better adaptability to the operating conditions.

3.9. *Comparison of H_2 purity at the outlet of the two systems*

By comparing and analyzing the hydrogen purity characteristics of the dual systems at the maximum efficiency operating condition under 0.7 MPa pressure (Fig. 10), the difference in the regulation of separation performance between the two system architectures is revealed.

The data show that: in the whole temperature range of 40–80 °C, the hydrogen purity of integrated systems always maintains above 99.5%, which has a significant advantage over traditional systems, indicating that the difference in system architecture has an essential difference in the ability to regulate product quality, and integrated systems has a better separation effect than traditional systems. The reason is that when the flow stock in the integrated system passes through the scrubber, the KOH in the flow stock will be removed, and the temperature of the flow stock will be reduced, and the separation efficiency will be improved in the gas-liquid separator, so that the purity of the product in the integrated system is significantly higher than that in the traditional system.

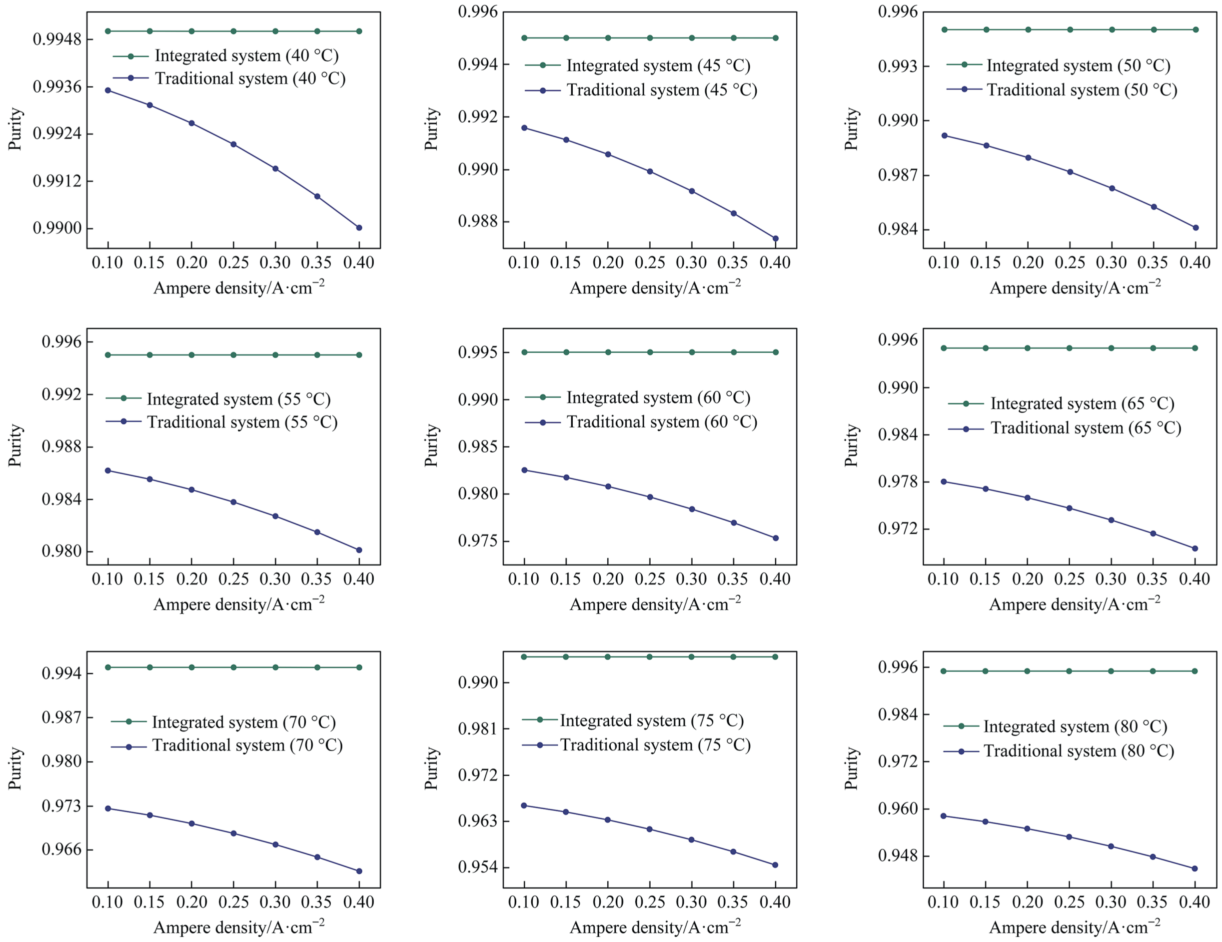

Fig. 10. Integrated system, traditional system outlet H_2 concentration.

4. Conclusions

This study addresses the critical challenge of gas entrainment in alkaline water electrolysis (ALK) systems through a novel integrated scrubbing-purification process and a multi-physics coupling model combining thermodynamic equilibrium and electrochemical dynamics. By establishing a comprehensive hydrogen production system model (2.5 $m^3 \cdot h^{-1}$ capacity), the synergistic effects of current density (0.1–0.4 $A \cdot cm^{-2}$), operating pressure (0.7–0.9 MPa), and temperature (40–80 °C) on system performance were rigorously investigated. The proposed integrated system demonstrates transformative improvements, achieving hydrogen purity exceeding 99.5%. A significant advancement over traditional systems (94.5%)—while maintaining comparable energy efficiency.

Key findings reveal that elevated temperatures enhance water conversion efficiency and reduce electrical demand, whereas higher current densities promote reaction kinetics at the expense of increased voltage and energy consumption. The scrubbing mechanism effectively eliminates KOH carryover, with gas-phase KOH concentrations approaching zero due to its high water solubility. Hydrogen purity exhibits an inverse correlation with temperature but improves with pressure, highlighting the importance of parameter optimization. Notably, the integrated system achieves a purity of 99.501% at optimal conditions (0.15 $A \cdot cm^{-2}$, 7 bar, 80 °C), with only a marginal efficiency difference (~0.03%) compared to conventional systems. A critical current density equilibrium point was identified, where system efficiencies converge and decay exponentially with rising temperature. Below 0.3 $A \cdot cm^{-2}$, the integrated system outperforms traditional setups in efficiency, while at higher current densities (>0.3 $A \cdot cm^{-2}$), efficiency parity is maintained despite auxiliary energy losses.

The Aspen Plus-based modeling framework proves invaluable for rapid thermodynamic analysis and operational parameter optimization, enabling precise balancing of energy efficiency and hydrogen purity. Although the integrated system exhibits a slight efficiency trade-off, its exceptional purity performance justifies its adoption in industrial settings prioritizing high-purity hydrogen for storage and transport. This work advances the design of alkaline electrolysis systems by resolving gas entrainment challenges and establishing a methodology for multi-parameter optimization. Future efforts should integrate techno-economic assessments to evaluate scalability and cost-effectiveness, further driving the development of sustainable, large-scale hydrogen production technologies. These insights provide a foundational roadmap for advancing next-generation electrolysis systems in alignment with global decarbonization goals.

CRediT Authorship Contribution Statement

Yufei Xie: Writing – original draft, Software, Investigation, Formal analysis, Data curation. Wu Qin: Writing – review & editing, Methodology, Investigation, Funding acquisition. Xianbin Xiao: Writing – review & editing, Supervision, Resources. Zongming Zheng: Writing – review & editing, Validation, Supervision, Resources.

Declaration of Competing Interest

The authors declare that they have no known competing financial interests or personal relationships that could have appeared to influence the work reported in this paper.

Acknowledgements

The authors wish to thank the National Key Research and Development Program of China (2023YFE0125500).

Nomenclature

A	area, m^2
C	parameter related to gas purity (temperature)
d	parameter related to ohmic resistance (pressure)
E	parameter related to gas purity (pressure)
f	parameter related to Faraday efficiency
F	faraday constant, 96485 $C \cdot mol^{-1}$
G	gibbs energy, $J \cdot mol^{-1}$
H	enthalpy, $J \cdot mol^{-1}$
I	current, A
i	current density, $A \cdot cm^{-2}$
N	number of cells of the stack
n	molar flow rate, $mol \cdot s^{-1}$
p	pressure, bar
Q	thermal power or heat transfer, W
r	parameter related to ohmic resistance (temperature)
S	entropy, $J \cdot mol^{-1} \cdot {}^{\circ}C^{-1}$
s	coefficient for overvoltage on electrodes, V
T	temperature, °C
t	coefficient for overvoltage on electrodes
V	voltage, V
W	electric power, $kJ \cdot h^{-1}$
z	electrons transferred per ion
η_F	efficiency,%

Subscripts

an	anode
cat	cathode
cell	alkaline water electrolysis cell
conc	concentration
ohm	ohmic
F	faraday
gen	generate or produced
prod	production
rev	reversible
stack	alkaline water electrolysis stack
th	theoretical or model
tn	thermoneutral

References

[1] A.M. Saleh, V. István, M.A. Khan, M. Waseem, A.N. Ali Ahmed, Power system stability in the era of energy transition: importance, opportunities, challenges, and future directions, *Energy Convers. Manag. X* 24 (2024) 100820.

[2] S.B. Yin, W.J. Jie, H. Wen, Research status and development prospects of hydrogen production technology in alkaline electrolyzer, *J. Xihua Univ. Sci. Ed.* 44 (2025) 168–180. . (in Chinese).

[3] F.A. Sulaiman, H. Sidiq, A.A. Ali, M. Mohamad, Mitigating liquid carry-over and foaming in a gas processing plant through the installation of vertical scrubbers, *Petrol. Chem.* 64 (1) (2024) 62–74.

[4] M. Kiaee, A. Cruden, P. Chladek, D. Infield, Demonstration of the operation and performance of a pressurised alkaline electrolyser operating in the hydrogen fuelling station in Porsgrunn, Norway, *Energy Convers. Manag.* 94 (2015) 40–50.

[5] G. Sakas, A. Ibáñez-Rioja, V. Ruuskanen, A. Kosonen, J. Ahola, O. Bergmann, Dynamic energy and mass balance model for an industrial alkaline water electrolyzer plant process, *Int. J. Hydrogen Energy* 47 (7) (2022) 4328–4345.

[6] Q. Hassan, A.Z. Sameen, H.M. Salman, M. Jaszczur, Large-scale green hydrogen production *via* alkaline water electrolysis using solar and wind energy, *Int. J. Hydrogen Energy* 48 (88) (2023) 34299–34315.

[7] D. Jang, H.S. Cho, S. Kang, Numerical modeling and analysis of the effect of pressure on the performance of an alkaline water electrolysis system, *Appl. Energy* 287 (2021) 116554.

[8] Y. Zheng, C.J. Huang, J. Tan, S. You, Y. Zong, C. Træholt, Off-grid wind/hydrogen systems with multi-electrolyzers: optimized operational strategies, *Energy Convers. Manag.* 295 (2023) 117622.

[9] R. Bhattacharyya, A. Misra, K.C. Sandeep, Photovoltaic solar energy conversion for hydrogen production by alkaline water electrolysis: conceptual design and analysis, *Energy Convers. Manag.* 133 (2017) 1–13.

[10] H. Shin, D. Jang, S. Lee, H.S. Cho, K.H. Kim, S. Kang, Techno-economic evaluation of green hydrogen production with low-temperature water electrolysis technologies directly coupled with renewable power sources, *Energy Convers. Manag.* 286 (2023) 117083.

[11] Y. Yang, B. De La Torre, K. Stewart, L. Lair, N.L. Phan, R. Das, D. Gonzalez, R.C. Lo, The scheduling of alkaline water electrolysis for hydrogen production using hybrid energy sources, *Energy Convers. Manag.* 257 (2022) 115408.

[12] S.H. Lee, Y. Kwon, S. Kim, J. Yun, E. Kim, G. Jang, Y. Song, B.S. Kim, C.S. Oh, Y.H. Choa, J.Y. Kim, J.H. Park, D.W. Jeong, A novel water electrolysis hydrogen production system powered by a renewable hydrovoltaic power generator, *Chem. Eng. J.* 495 (2024) 153411.

[13] M.H.A. Aboukalam da Cruz, M. Etancelin, F. Marias, J.M. Reneaume, S. Sochard-Reneaume, S. Serra, Dynamic modelling of an alkaline water electrolysis system and optimization of its operating parameters for hydrogen production, *Int. J. Hydrogen Energy* 48 (35) (2023) 12982–12999.

[14] F. Lai, M.Y. Wang, J.Z. Zhou, J. Song, Y.P. Yuan, Hybrid PV-PV/T driven proton exchange membrane water electrolysis systems for hydrogen production: experimental investigation and the role of thermal management, *Energy Convers. Manag.* 344 (2025) 120326.

[15] H.R. Zhou, X. Wu, C.L. Li, S.Y. Yang, Z.C. Chen, J. Lu, C. Fang, Optimization of capacity configuration and comprehensive evaluation of a renewable energy electrolysis of water for hydrogen production system, *Chin. J. Chem. Eng.* 76 (2024) 301–317.

[16] X.Y. Huang, H.K. Jeswani, A. Azapagic, Sustainability assessment of hydrogen production *via* water electrolysis considering different configurations of solar photovoltaics-battery-grid systems in China, *Sustain. Prod. Consum.* 56 (2025) 221–244.

[17] W.W. Xu, L.L. Yang, Z.Q. Niu, S. Wang, Y.L. Wang, Z.Y. Zhu, P.Z. Cui, Thermodynamic and economic analysis of a novel DME-power polygeneration system based on the integration of biomass gasification and alkaline electrolysis of water for hydrogen production, *Energy* 314 (2025) 134185.

[18] F.Z. Wang, Y.Y. Li, Waste heat-driven biogas cogeneration-methanol synthesis system: assessment of the coupling of carbon dioxide methanolisation and hydrogen production from water electrolysis, *Fuel* 402 (2025) 136059.

[19] X.H. She, C. Feng, D.L. Liu, Z.Y. Fan, M.J. Yang, Y.B. Li, A stable alkaline anion exchange membrane water electrolyzer based on a self-healing anode, *Int. J. Hydrogen Energy* 59 (2024) 1297–1304.

[20] A. Meena, P. Thangavel, D.S. Jeong, A.N. Singh, A. Jana, H. Im, D.A. Nguyen, K. S. Kim, Crystalline-amorphous interface of mesoporous $Ni_2P@FePO_xH_y$ for oxygen evolution at high current density in alkaline-anion-exchange-membrane water-electrolyzer, *Appl. Catal. B Environ.* 306 (2022) 121127.

[21] Nur Nadhirah Syafiqa Binti Mohammad Musa, A.S. Tijani, Effect of exchange current density and charge transfer coefficient on performance characteristics of voltage of alkaline electrolysis, *Appl. Energy* 394 (2025) 126186.

[22] P.C. Zhao, J.G. Wang, L.M. Sun, Y. Li, H.T. Xia, W. He, Optimal electrode configuration and system design of compactly-assembled industrial alkaline water electrolyzer, *Energy Convers. Manag.* 299 (2024) 117875.

[23] M. Plevová, J. Hnát, J. Žitka, L. Pavlovec, M. Otmar, K. Bouzek, Optimization of the membrane electrode assembly for an alkaline water electrolyser based on the catalyst-coated membrane, *J. Power Sources* 539 (2022) 231476.

[24] P. Olivier, C. Bourasseau, P.B. Bouamama, Low-temperature electrolysis system modelling: a review, *Renew. Sustain. Energy Rev.* 78 (2017) 280–300.

[25] M. Sánchez, E. Amores, L. Rodríguez, C. Clemente-Jul, Semi-empirical model and experimental validation for the performance evaluation of a 15 kW alkaline water electrolyzer, *Int. J. Hydrogen Energy* 43 (45) (2018) 20332–20345.

[26] J. Barco-Burgos, U. Eicker, N. Saldaña-Robles, A.L. Saldaña-Robles, V. Alcántar-Camarena, Thermal characterization of an alkaline electrolysis cell for hydrogen production at atmospheric pressure, *Fuel* 276 (2020) 117910.

[27] E. Amores, J. Rodríguez, J. Oviedo, A. de Lucas-Consuegra, Development of an operation strategy for hydrogen production using solar PV energy based on fluid dynamic aspects, *Open Eng.* 7 (1) (2017) 141–152.

[28] P. Haug, M. Koj, T. Turek, Influence of process conditions on gas purity in alkaline water electrolysis, *Int. J. Hydrogen Energy* 42 (15) (2017) 9406–9418.

[29] S. Pöyhönen, A. Ibáñez-Rioja, G. Sakas, A. Kosonen, V. Ruuskanen, P. Kauranen, J. Ahola, J. Kiilavuo, A. Krimer, Dynamic mass- and energy-balance simulation model of an industrial-scale atmospheric alkaline water electrolyzer, *Energy* 322 (2025) 135602.

[30] Z. Abdin, C.J. Webb, E.M. Gray, Modelling and simulation of an alkaline electrolyser cell, *Energy* 138 (2017) 316–331.

[31] Y.H. Zhuo, W.Z. Zhang, Y.X. Luo, P.X. Hao, Y.X. Shi, Progress of elevated-temperature alkaline electrolysis hydrogen production and alkaline fuel cells power generation, *J. Fuel Chem. Technol.* 53 (2) (2025) 231–247.

[32] E. Amores, J. Rodríguez, C. Merino, P. García Escribano, Influence of operation parameters in the modeling of alkaline water electrolyzers for hydrogen production, *Int. Hydro. Energy* 39 (24) (2014) 13063–13078.

[33] B. Karthikeyan, G. Praveen Kumar, S. Basa, S. Sinha, S. Tyagi, P. Kamat, R. Prabakaran, S.C. Kim, Strategic optimization of large-scale solar PV parks with PEM Electrolyzer-based hydrogen production, storage, and transportation to minimize hydrogen delivery costs to cities, *Appl. Energy* 377 (2025) 124758.

[34] S.L. Ding, B. Guo, S. Hu, J.J. Gu, F.Y. Yang, Y.Y. Li, J. Dang, B. Liu, J.G. Ma, Analysis of the effect of characteristic parameters and operating conditions on exergy efficiency of alkaline water electrolyzer, *J. Power Sources* 537 (2022) 231532.